

Airborne Sense and Detect of Drones using Deep Learning and LiDAR Point Clouds

Manduhu Manduhu, Alexander Dow, Petar Trsllic, Gerard Dooly, Benjamin Blanck, James Riordan



Abstract—The safe operation of drone swarms beyond visual line of sight requires multiple safeguards to mitigate the risk of collision between drones flying in close-proximity scenarios. Cooperative navigation and flight coordination strategies that rely on pre-planned trajectories, constant network connectivity and reliable Global Navigation Satellite System (GNSS) positioning are brittle to failure. Drone embedded sense and detect offers a comprehensive mode of separation between drones for deconfliction and collision avoidance. This paper presents the first airborne LiDAR based solution for drone-swarm detection and localization using 3D deep learning model. It adapts an existing deep learning neural network to the air-to-air drone scenario by expanding the scan space vertically. A new sparse convolution is proposed and applied to accelerate the backbone layer, which is the most time-consuming part of the neural network. To collect training data of safety critical, close-proximity multi-drone operations, a scenario Digital Twin is used to augment real datasets with high fidelity synthetic data. The trained model achieves over 80% recall and 96% precision when tested on real-world datasets. By incorporating a tracking-by-detection algorithm the system can reliably monitor the separation distance of multiple drones in challenging environments.

Index Terms—sense-and-detect, drone swarm, deep learning, sparse convolution, digital twin.

1 INTRODUCTION

SENSE and detect, which involve identifying and responding to potential conflicts, are crucial for estimating risks in dynamic drone swarm environments [1]. As drone use cases expand, it becomes essential to validate technologies that can take on the safety-critical role of onboard pilots by monitoring surrounding airspace for hazards, including air and ground collision risks. Current drone swarm management systems rely primarily on trajectory-based flight planning, where predefined flight paths guide drones to avoid conflicts. Simultaneous Localization and Mapping (SLAM), which enables drones to build a map of their environment and track their position within it, along with anti-spoofing techniques that protect against falsified GPS signals, have improved in-flight positional estimation and

broadcast. However, tactical deconfliction—the process of managing and resolving potential flight path conflicts—still depends on centralized decision-making and continuous connectivity to a command and control (C2) center. This centralized system is vulnerable to network failures, and it relies on cooperative behavior from all airborne vehicles. Faulty or uncooperative traffic can enter the flight space undetected, posing risks. To safeguard users and mitigate air-to-air collision risks, onboard drone-embedded sense and detect capabilities, where drones autonomously perceive and avoid conflicts, are necessary.

This paper addresses the challenge of monitoring a drone swarm while they perform a collaborative mission, such as a maintenance-inspection survey. The integrated system can effectively monitor the separation distance between multiple drones in challenging environments and alert for potential air-air collisions between drones. The paper describes the first drone-embedded system that uses point-based artificial intelligence for detection and localization of other drones. We adapt an existing detection model, originally designed for ground applications such as autonomous vehicles, to an air-to-air drone scenario by expanding the scan space vertically. To reduce the latency of the detection model, we introduce a new sparse convolution algorithm that leverages the sparsity of LiDAR data. This algorithm is applied to accelerate the backbone layer of the model, which is the most time-consuming component of the detection process.

Currently, drones present challenges in the AI domain, characterized by a lack of high-quality data for training and validating hazard perception algorithms, coupled with an absence of data sharing mechanisms that can handle sensitive and privacy constrained hazard observation data. We develop a blended reality data augmentation strategy that outperforms conventional data augmentation strategies by adapting a scenario Digital Twin of the operating scenario and equipping the virtual environment with high fidelity drone and LiDAR simulators. Our results demonstrate that detection models trained on high-fidelity synthetic augmentation datasets outperform those trained on conventional augmentation datasets.

Our contributions are:

- 1) We propose the first airborne LiDAR based solution for drone-swarm detection and localization using 3D deep learning, which considers critical factors of real-time sense and detect of drones for safety scenarios.

Manduhu Manduhu, James Riordan, and Alexander Dow are with the Drone Systems Lab, School of Computing, Engineering, and Physical Sciences, University of the West of Scotland, Glasgow, Scotland.

Corresponding author: James Riordan (email: james.riordan@uws.ac.uk).

Petar Trsllic and Gerard Dooly are with the Centre for Robotics & Intelligent Systems, Department of Electronic & Computer Engineering, University of Limerick, Limerick, Ireland.

Benjamin Blanck is with Hamburg Port Authority, Hamburg, Germany.

We adapt an existing detection model for an air-to-air drone scenario by expanding the scan space vertically.

- 2) We propose a novel sparse convolution algorithm to accelerate the backbone layer of the detection model, achieving a speedup factor of 2.3.
- 3) To further improve detection accuracy, we employ a synthetic data augmentation strategy for training data generation. The model trained on this dataset achieves the highest performance with 80% recall and a 96% precision. The model, trained on real-world data, achieves a recall of 62% and a precision of 82.6%.

2 RELATED WORK

In the context of drone conflict avoidance, sense and detect can be defined as follows: Sense refers to the methods employed by a drone to actively gather information about its surrounding environment. These methods typically involve onboard sensor technologies, such as cameras, LiDAR, and other advanced sensing systems. Detect involves analyzing the data collected by the drone's sensors. The analysis aims to identify the presence of threats and hazards within the drone's operational space and assess the potential and severity of these threats to the drone's safe operation.

2.1 Detection and Tracking of Drones

2.1.1 Data collection using various sensors

An exploration [2] is conducted to examine the distinctive marks of small Unmanned Aerial Vehicles (UAVs) utilizing a variety of sensor technologies. These technologies include acoustical antennas, passive and active optical imaging tools, as well as compact FMCW RADAR systems. As described in [3], acoustic-based detection of UAVs utilizing various machine learning algorithms offers a promising approach for UAV identification. However, this method inherently faces limitations in precise localization in 3D space which is critical requirement in our use case. While [4] presents a method for single-drone detection using passive radio frequency (RF) signals, this technique is less effective for drone swarms. The presence of multiple drones operating in the same area (as in our use case) elevates the overall background RF noise level, hindering the ability of RF-based detection systems to isolate and identify the weaker signals from individual drones within the swarm.

Radar technology [5][6][7] presents a valuable approach for drone detection, though its effectiveness is hampered by the low radar cross-section (RCS) of drones. This limitation can lead to missed detections, particularly for smaller drones, significantly restricting its use in safety-critical applications such as our use case involving drone swarm monitoring. Several camera-based detect and track of small UAVs are presented in [8][9][10][11]. Camera-based UAV detection offers an efficient solution for verification and classification of drones, however, their performance is significantly impacted by environmental factors like lighting conditions and weather. Additionally, cameras inherently provide only 2D information, lacking the crucial depth data required for precise 3D localization, which is essential for our needs.

A complete chain of detection, tracking, and classification of small flying objects in real-time is presented in

[12]. This is achieved through the use of a mobile multi-sensor platform equipped with two 360° LiDAR scanners and pan-and-tilt cameras in the visible and thermal infrared (IR) spectrum. The approach involves the initial detect and track of flying objects in 3D LiDAR data. After localizing, the cameras are automatically directed to the object's position, and each sensor records a 2D image. A convolutional neural network (CNN) is then used to identify the region of interest (ROI) and classify the object into one of eight different types of UAVs and birds. Clearly this two-stage detection and classification approach will introduce higher latency. Alongside latency issues, deploying this system on a drone poses further challenges due to the weight and power limitations inherent in drone platforms.

As UAVs have gained popularity, the attention towards cooperative UAV detection and tracking has intensified. To improve cooperative UAV navigation in GNSS-challenging conditions, the approach presented in [13] combines camera based measurements with navigation data from other aircraft flying under better GNSS coverage. Clearly, this approach is not independent of external aiding systems. External aiding systems, such as GNSS, can introduce multipath errors caused by signals reflecting off buildings, trees, the ground, and other surfaces.

This paper presents the first airborne LiDAR based solution for drone detection using point-cloud based 3D deep learning network. This approach represents an advancement in drone detection technology, as it satisfies different requirements for real-time sensing and detection of drones in safety critical scenarios.

2.1.2 Deep learning on points clouds

Recently deep learning on point clouds has become a prevalent AI technique in autonomous driving. Numerous methods have been proposed to address different problems in this area. A comprehensive review of deep learning approaches on point clouds is presented in [14]. As a pioneering work on point clouds classification and segmentation, PointNet [15] and its successor PointNet++ [16] has inspired many others works in this area.

VoxelNet [17] organizes point clouds into evenly spaced 3D voxels and applies a PointNet to encode point-wise features within each voxel. A 3D convolutional middle layer and a region proposal network are then applied to generate 3D object proposals in the form of 3D bounding boxes. The computational bottleneck resides in the 3D convolution layer. SECOND [18] improved VoxelNet by applying sparse convolution and achieved an inference speed of 30.4 FPS [19] on a NVIDIA RTX 2080 Ti GPU, but the 3D convolutions remain a bottleneck. PointPillars [20] enables end-to-end learning with only 2D convolutional layers. It divides the x-y coordinate plane into evenly spaced grid cells and organizes point clouds into the corresponding cell to create "pillars". A simplified PointNet is applied the points within pillars. The backbone network consisting of multiple 2D convolutions is then applied to pseudo-image of features generated from the processed pillars. A detection head [21] is then used to generate 3D bounding box for objects in point cloud data. The inference of PointPillars can run at a speed of 42.4 FPS. Therefore it is highly suitable for applications requiring real time processing.

PV-RCNN [22] extends SECOND by adding a keypoints branch to preserve 3D structural information. Its backbone network takes the raw point cloud data as input to extract point-wise features. PV-RCNN can achieve a higher accuracy but its inference speed is only 8.9 FPS, which falls below real-time requirements. Voxel-RCNN [19] further improves accuracy by leveraging a 3D network for feature extraction. It then applies a 2D backbone network and Region Proposal Network (RPN) to BEV representation of the 3D feature volumes. Its inference achieves the speed of 25.2 FPS.

While there are various 3D object detection networks that can achieve higher detection performance, we selected PointPillars for our work due to its real-time inference capability; it consistently achieves the highest FPS compared to other detection models [19]. This is a critical consideration for our use-case application, which is safety orientated and requires the ability to process incoming point clouds in real time. While higher detection performance is desirable, it often comes at the cost of increased computation time and resource requirements, which can limit the feasibility of deploying the network in real-world application scenarios. We chose PointPillars as a balance between detection performance and real-time inference capability to meet the requirements of our drone detection applications.

Instead of purely using the original PointPillars network, we modify it for an air-to-air drone scenario by extending the scan space vertically. To reduce inference latency, we propose a new sparse convolution algorithm to accelerate the backbone layer, which is the most time-consuming part of PointPillars [23].

2.2 Latency Reduction

While increasing the number of point clouds can improve detection accuracy, minimizing latency is crucial for ensuring real-time hazard response. The inherent sparsity of LiDAR data can be utilized to reduce latency. The study in [24] describes the spatial sparsity of feature maps and how sparsity applies to improve performance of different applications. A sparse convolutional neural network that utilizes sparse matrix multiplication is presented in [25]. An efficient sparse convolutional operation called submanifold sparse convolution is introduced in [26], in which the output will be computed if and only if the corresponding site in the input is active.

Matrix multiplication is an efficient method for implementing spatial convolution on GPU, as demonstrated by [27]. This requires transforming the input image into matrices that are suitable for fast multiplication. This transformation can be achieved by lowering the input data with duplication. The GPU implementation of the proposed method in this paper is also based on fast GPU matrix multiplication, but without data lowering.

A sparse convolution with rule book is presented in [18], where the rule book is used to map between input and output. The work presented in [28] generalizes convolution, including sparse convolution, to handle any discrete convolutions in high-dimensional spaces. A highly efficient Sparse Kernel Generator is developed in [29], which produces high performance sparse point cloud convolution kernels at a fraction of the engineering cost of the current state-of-the-art.

Most current methods implement convolution as a gathering operation, where neighboring pixels are multiplied by corresponding filter elements, and the results are summed to update the center pixel. Sparse convolution implementations typically follow this approach as well. To accelerate GPU performance, a hash table or rule book is often used to map positions between the input and output. In this paper, we propose an alternative approach to implementing sparse convolution using a scattering operation. This method eliminates the need for a hash table or rule book, improving efficiency while simplifying the implementation.

2.3 Training Data Generation

Within the context of autonomous driving, there are different datasets such as KITTI [30], Waymo Open [31] and nuScenes [32] and others which are available online, and include LiDAR as part of the dataset. These datasets contain a collection of diverse urban scenes and dense position and class annotations. These datasets provide us with valuable resources for validating autonomous driving algorithms, enabling the development of more accurate and robust perception systems.

Whilst these datasets are useful, in reality, it is impossible to test and improve autonomous driving systems in all potential real-world scenarios. Simulation of the perception system and the physical world becomes an important approach for testing and improving the safety of autonomous driving. Indeed, it was shown [33][34][35][36][37] that simulation-based approaches can achieve state-of-the-art results when autonomous driving models were trained on synthetic data.

LiDAR is one of the most important sensors for autonomous driving and many works have focused on the simulation of LiDAR. In [38][39], a LiDAR simulator which can augment real point clouds with synthetic objects is implemented. The real point cloud (usually a background) is generated from real LiDAR scanners mounted on top of a vehicle sweeping real world surroundings. The point cloud of a synthetic object is obtained by scanning handcraft CAD models with virtual LiDAR. These works demonstrate the importance of position and orientation of scanning objects for detection and segmentation. A LiDAR simulation approach described in [40] leverages real-world data to enhance the realism of the simulated scenes. This approach results in more diversity and realism in the simulated scenes. It also describes a learning system that models the residual physics that are not captured by graphics rendering, which further boosts the realism of the simulation. For a drone usage scenario, the study in [41] employs LiDAR simulation to evaluate the performance of detect-and-avoid systems for unmanned aerial systems (UAS).

In this work, we enrich the AI training dataset by using a Digital Twin to accurately simulate a LiDAR sensor and augment the simulated point clouds within a real-world background. Unlike conventional augmentation techniques, our approach reflects the actual position and orientation of the scanned object.

3 DETECTION MODEL

We modify the PointPillars model for air-to-air drone scenarios by extending the scan space vertically. Furthermore,

we introduce a novel sparse convolution algorithm to accelerate the detection model’s backbone layer.

3.1 Original PointPillars

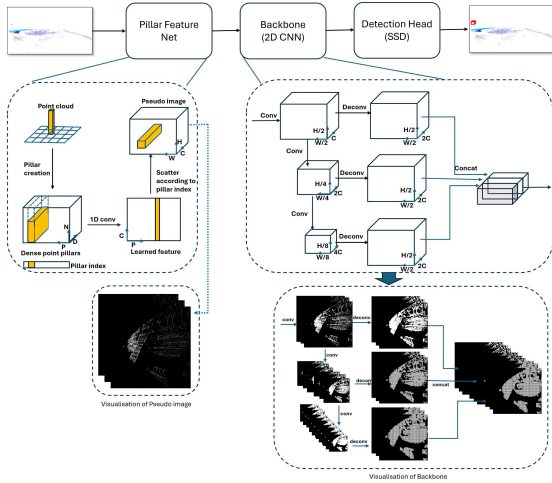


Fig. 1: The PointPillars architecture consists of three key building blocks: Pillar Feature Net, Backbone, and Detection Head. The lower section visualizes binary images of various stages of the backbone in the latent space.

PointPillars is a deep learning-based object detection algorithm originally designed for autonomous driving applications on ground. It can operate on 3D point clouds generated by LiDAR sensors. As shown in Fig. 1, the PointPillars network consists of three main components: the voxelization layer (pillar feature net), the backbone layer, and the detection head. The voxelization layer takes raw point cloud data as input and converts it into a sparse 3D voxel grid representation. The voxel grid is organized into pillars, which are vertical stacks of voxels that preserve the spatial and geometric information of the original point cloud data. The feature dimension of each point is denoted by D , encompassing nine dimensions: the spatial coordinates x , y and z ; reflectance r ; the pillar centre offset values x_p and y_p ; and the distance to the arithmetic mean of the pillar x_c , y_c and z_c . Points within each pillar are first processed through a 1D convolution block. The maximum values from each pillar are then taken as features and scattered to their corresponding positions on the 2D pseudo-image of the pillar grid. The backbone layer is a convolutional neural network (CNN) that takes as input the features of the points in each pillar and extracts high-level semantic features that capture the spatial and semantic characteristics of the objects in the point cloud data. The backbone layer is the most computationally expensive part of the detection model. The detection head takes as input the features extracted by the backbone layer and generates a set of predicted 3D bounding boxes for each object in the point cloud data. The detection head is a two-stage network that first predicts the objectness score for each voxel in the point cloud data and then refines the location and size of each predicted box.

3.2 Adaptations to Drone Scenarios

In autonomous driving applications the LiDAR sensor is mounted on top of a vehicle and the point cloud data is collected from a ground-level perspective. In airborne sense and detect, the LiDAR sensor observes the full 3D space, with objects of interest frequently appearing above and below the horizontal plane of the drone-mounted LiDAR. Our use case (maintenance inspection survey) involves flight below the 120m ceiling (due to regulations) and is typically less than 60m to meet the data resolution and ground sample density requirements of the survey specification. An example of a LiDAR point cloud (accumulated) generated by an airborne survey with a drone is shown in Fig. 2. While the original network was trained to detect multiple classes of object (cars, pedestrians, etc.) we focused on a single object class and annotated only observations of drones in the point cloud data.



Fig. 2: Reconstructed LiDAR point clouds generated by an airborne survey with a drone

In the PointPillars architecture, the 3D space is divided into a set of pillars, and each pillar corresponds to a 2D slice of the 3D space. The anchors are predefined 3D bounding boxes that are used to classify and regress the objects within each pillar. By default, the PointPillars algorithm uses a fixed-size anchor boxes and z-center of anchor boxes is usually fixed at a constant value, since the elevation of the object being detected is assumed to be relatively constant in the local area covered by the LiDAR sensor. PointPillars performs object localization by first regressing the object’s position in the X-Y plane, followed by additional regression steps to determine height and elevation.

To better detect airborne objects such as drones with varying elevation, we made the following adaptation to the original PointPillars. We horizontally stratify the LiDAR field of view into layers where each layer extends to 1m in height (typically 10 layers above and 10 layers below the elevation of the LiDAR). We allocate an anchor box of size $1.6m \times 1.6m \times 1.0m$ (length \times width \times height) to each layer, with the centre of the anchor box located at the centre of each layer. We also assign different class names to each layer, such as from $drone_0, drone_1, \dots, drone_{20}$. Each class has a corresponding anchor box. The optimal elevation prediction will be related to both the z-centre localization accuracy and the classification accuracy. As shown in the original PointPillars, the localization regression residual along the z-axis is given by Equation 1, where z^{gt} and z^a are the z-centre of ground truth box and anchor box respectively, h^a

is the height of the anchor box. The object classification loss is given by Equation 2, where p^a is the class probability of an anchor, α and γ are parameters used to adjust the loss function in order to address class imbalance,

$$\Delta z = \frac{z^{gt} - z^a}{h^a} \quad (1)$$

$$L_{cls} = -\alpha_a(1 - p^a)^\gamma \quad (2)$$

here α and γ are set to constants of 0.25 and 2 respectively as in the original PointPillars.

This approach allows the algorithm to better detect objects with varying elevation, such as a drone. The size and spacing of the layers are determined based on the characteristics of the drone being detected. We use the same loss functions introduced in the original PointPillars.

It is important to note that adding more layers along the z-axis may increase the computational cost of the algorithm. Therefore, it is important to balance the number of layers with the performance requirements of the application. A trade-off between accuracy and speed should be considered when selecting the number of layers.

3.3 Optimization

We propose a new algorithm for sparse convolution and apply it to accelerate the backbone layer, which is the most computationally expensive part of the detection model.

3.3.1 Sparse convolution with scatter operation

We describe the convolution with scatter operation first. With standard convolution, at each output location, the product between each element of the filter and the input element it overlaps with is computed and the results are summed to obtain the output in the current location, see Fig. 3a and 3b. However, in standard convolution, observe that the same input element multiplied by different filter weights contributes to different output elements and the location of those output elements neighbor each other. For example, in Fig.3b, the input element x_{13} is multiplied by different filter weights and the results are added to different output locations. Specifically, $x_{13} \times w_9$ is added to the location of y_7 , $x_{13} \times w_8$ is added to the location of y_8 and so on. We can implement the convolution in an alternative way: multiply each input element with different filter weights and add the result to each corresponding output location which is decided by the filter weight location, see Fig. 3c. We call this implementation **Convolution with Scatter Operation** (Unlike standard convolution in which each neighboring pixel is multiplied by the corresponding filter weight and the result is added to the final output position, in this proposed convolution, each pixel is multiplied by different filter weights and the results are added to different output positions. Therefore we call it the Convolution with **Scatter Operation**).

Given an input image I with size of $p \times q$, a filter W with size of $k \times k$ and the output image O , the general formula of the convolution with scattering operation is given as follows:

$$O_{i-m+[k/2],j-n+[k/2]} += I_{i,j} \times W_{m,n} \quad (3)$$

$$m \in \{0, \dots, (k-1)\}, n \in \{0, \dots, (k-1)\}$$

$$i \in \{0, \dots, (p-1)\}, j \in \{0, \dots, (q-1)\}$$

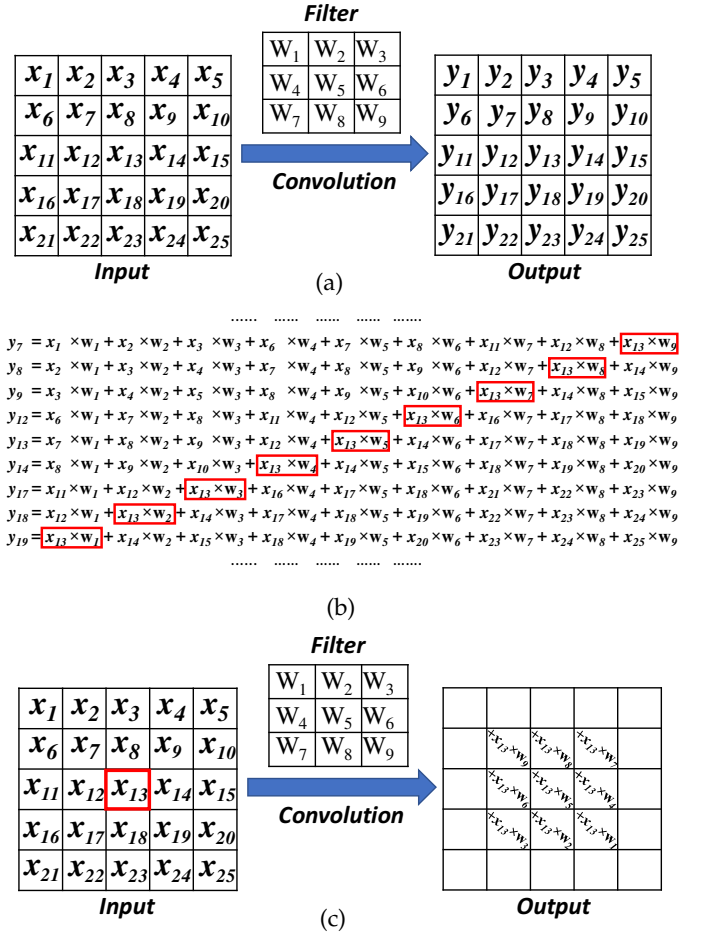


Fig. 3: (a) Standard convolution where x_i, w_i, y_i represent the input, filter and output, respectively. (b) Computation of each output y_i ; It also shows how x_{13} is involved in the computation of these output elements. (c) The proposed Convolution with Scatter Operation.

For the input image with C channel, the convolution with scattering can be expressed as follows:

$$O_{i-m+[k/2],j-n+[k/2]} += \sum_{c=0}^{c=C-1} I_{i,j,c} \times W_{m,n,c} \quad (4)$$

$$m \in \{0, \dots, (k-1)\}, n \in \{0, \dots, (k-1)\}$$

$$i \in \{0, \dots, (p-1)\}, j \in \{0, \dots, (q-1)\}$$

Obviously, the sparse convolution can be implemented by applying the scatter operation to each active site (non-zero site) only.

The psudo code of the convolution with scatter operation is given in Algorithm 1. It is clear the number of multiplications and additions required is the same as standard convolution, it is $O(p \times q \times k^2)$. For sparse convolution with scatter operation, the time complexity is $O(l \times k^2)$ where l is the number of active sites and $l \ll p \times q$.

3.3.2 GPU implementation

The convolution operation can be efficiently implemented on GPU using matrix multiplication, as shown by [27]. This approach requires transforming the input image and the

Algorithm 1: Convolution with scatter operation

Input: An image $I(i, j)$ of size $p \times q$ and a filter $W(m, n)$ of size $k \times k$
Output: A new image $O(x, y)$ after convolution
for $i \leftarrow 0$ **to** $p - 1$ **do**
 for $j \leftarrow 0$ **to** $q - 1$ **do**
 for $m \leftarrow 0$ **to** $k - 1$ **do**
 for $n \leftarrow 0$ **to** $k - 1$ **do**
 $x \leftarrow i - m + \lfloor k/2 \rfloor$;
 $y \leftarrow j - n + \lfloor k/2 \rfloor$;
 $O(x, y) \leftarrow O(x, y) + I(i, j) \times W(m, n)$;
 end
 end
 end
end
return $O(x, y)$;

convolution kernel into matrices that can exploit the fast multiplication capabilities of the GPU. This transformation involves duplicating the input data to lower its dimensionality.

In our GPU implementation of Sparse Convolution with Scatter Operation, we use matrix multiplication to perform the channel-wise multiplication and summation of the input and a filter kernel. To achieve a higher performance, we first use the GPU prefix sum [42] to compress the active sites in the input image into a dense format. Positions of all active sites are recorded in a 2D mask array, where an element of the 2D array is set to 1 if the corresponding site is an active site, otherwise it is set to 0. The prefix sum will then be applied to this 2D mask array. NVIDIA cuBLAS library [43], a library of highly optimized matrix multiplication routines, is used to perform the channel-wise multiplication and summation. The results are then scattered to the corresponding output positions according to the scattering rule. To avoid write conflicts, we use the atomicAdd() function [44] to perform the final addition. Unlike the method in [27], we do not apply any data lowering in our GPU implementation. Additionally, there is no the rule book or hash table used in our GPU implementation, as rule book or hash table increases the memory overhead and the computation complexity.

In this work, we present the initial implementation of the Sparse Convolution with Scatter Operation. Our GPU implementation follows gather-GEMM-scatter dataflow [29], which needs to read and write DRAM at least three times, respectively. There is significant room for optimization using the following techniques: 1) perform computation on on-chip SRAM (shared memory) using tiling, which reduces access to DRAM memory, and 2) overlap memory access with computation.

4 MODEL TRAINING

Our training and testing workflows incorporate the requirements of the Specific Operation Risk Assessment [45]. The methodology involves 5 steps:

- 1) The operational site is mapped by a drone mounted LiDAR. The LiDAR is oriented in forward looking

mode to capture point cloud data for the monitoring scenario. During the mapping flights, multiple drones are flown in controlled patterns within the segregated airspace and under supervision. The observations of these drones in the LiDAR point cloud data are labelled using the recorded position and navigation data of each drone in the swarm to generate an annotated training dataset. With the help of GPS correction techniques such as Real Time Kinematics (RTK) and Post Processed Kinematics (PPK), we achieve a high-quality annotation in which the error can be controlled $< 5cm$.

- 2) The annotated point data is augmented by inserting additional synthetic LiDAR data of drones in simulated safety critical scenarios.
- 3) The blended reality dataset is used to train the model.
- 4) Model performance is measured using real LiDAR data. Identified shortcomings are used to refine the training and model parameters and define strategic mitigations during mission planning, for example exclusion zones that might be challenging the model accuracy.
- 5) The trained model is embedded on the drone and deployed for tactical monitoring of drones within the operating theatre.

4.1 Training Data Collection and Labelling

Collection of the training and testing datasets utilized two different LiDAR systems. Server-based training and lab testing used data collected with a DJI L1 LiDAR [46], while the Livox Avia LiDAR [47] is used to test the real-time embedded model on the drone. The systems are interchangeable as the L1 package contains a Livox Avia module, whilst incorporating an IMU and an active gimbal to compensate for motion disturbance and enable accurate recording of point data in absolute coordinates. However, the L1 does not support real-time data access and thus can not be used in sense and detect modes of operation.

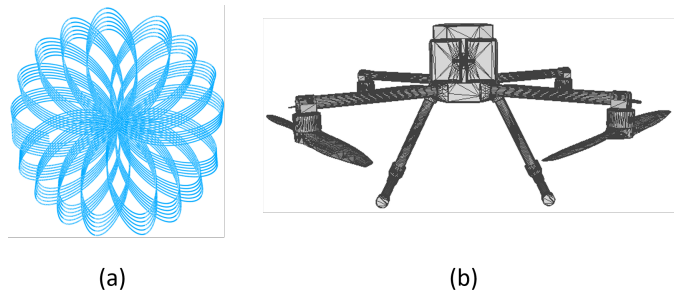


Fig. 4: (a) Livox Avia non-repetitive scanning pattern (100ms frame) (b) The wireframe mesh model of the M300, which is defined by 207409 triangular facets.

The Avia generates 240k points per second with two options for scanning mode. The repetitive line scanning is 70.4° (horizontal) $\times 4.5^\circ$ (vertical) and is best suited for mapping in downward looking configuration while the drone moves forward. The alternative non-repetitive scanning pattern (see Fig. 4(a)) is 70.4° (horizontal) $\times 77.2^\circ$ (vertical) and is preferable for monitoring airspace.

L1 data exchange is supported by converting the raw LiDAR data into the interoperable LAS format (v1.2) and

Smoothed Best Estimate (SBET) files for 3D reconstruction in EGM96 geoid. The observations of swarm drones can then be labelled with bounding boxes calculated from the recorded flight logs. For each point, the LAS (Point Record Format 3) records the relative coordinate X , Y , Z and reflectivity along with the GNSS timestamp at microsecond precision. The SBET file provides the timestamped 6 degree-of-freedom LiDAR pose information throughout the flight enabling transformation of the LAS point data between body, earth, and PointPillars coordinate systems. In the case of the real-time stream from the Avia, the data is already in body fixed frame aligned to the PointPillars coordinate system. Example frames (100ms frame) with swarm drone labelled are shown in Fig. 5.

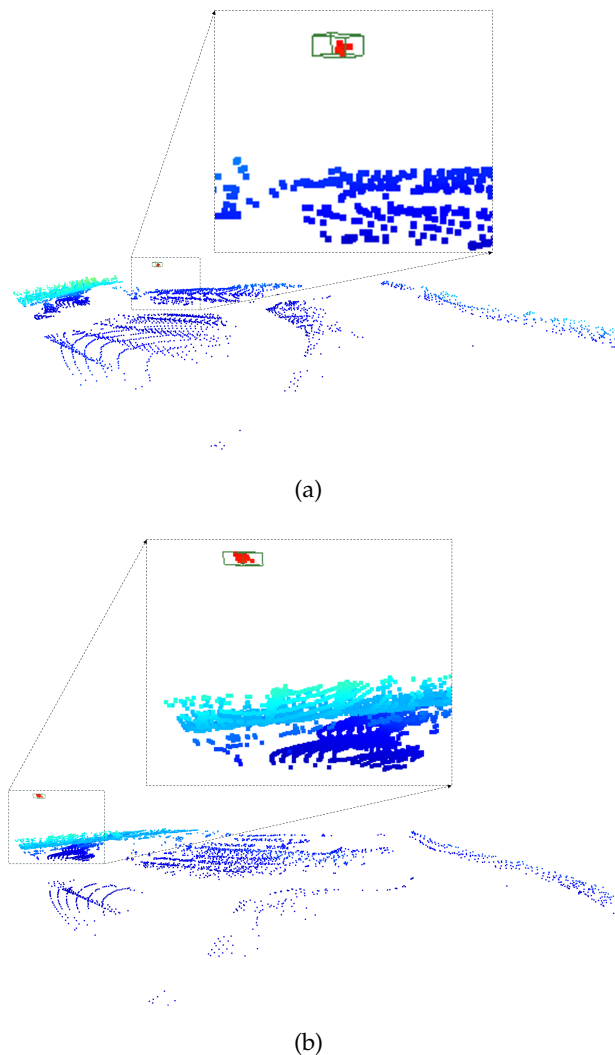


Fig. 5: A lateral view of a 100ms frame of LiDAR data, showing a swarm drone labeled with a green box. A portion of the frame containing the drone is enlarged for clarity. (a) The distance between the LiDAR and the swarm drone is 13.51m. (b) The distance between the LiDAR and the swarm drone is 46.58m.

4.2 Data Augmentation

As described in Section 3, the robustness of the detection model relies on the geometric and spatial variation in the

point cloud. However, obtaining point clouds from every position of the field of view of a LiDAR sensor is, in reality, not feasible. To address this limitation, training data augmentation is commonly employed.

Conventional data augmentation strategies expand the training dataset by applying fixed transformations, such as rotation, scaling, and translation, to the original labeled objects. However, due to the 3D spatial characteristics of point clouds, it is possible that the LiDAR may never generate an augmented point cloud from its viewpoint in the physical world. Especially when the LiDAR employs a non-uniform scan pattern (non-repetitive pattern). The LiDAR never generates a point cloud that matches the rotation-augmented or translation-augmented points from its view point. Also, unlike camera images, the scale of a 3D point cloud remains constant regardless of the distance between the LiDAR sensor and the object being scanned. This potentially results in learned features from augmented data that contribute less or even negatively to the model's overall performance. For a drone usage scenario, the study in [41] employs LiDAR simulation to evaluate the performance of detect-and-avoid systems for unmanned aerial systems (UAS).

Our augmentation strategy instead uses a scenario Digital Twin to accurately model the relationship between the relative positions of the LiDAR and observed drones and the heterogeneous spatial and temporal resolution of the LiDAR sensor. The simulated points generated by the Digital Twin exhibit a sampling pattern and sensing distortion that matches its relative location within the LiDAR field of view. Fig. 6 shows the simulated drone cluster generated by ray tracing a triangulated model of the M300 drone at different locations within the LiDAR field of view. Simulation of 100ms frames takes an average 0.2075ms on an 8 GPU server. This involves ray tracing a drone model with 207,409 triangles. In effect the simulator can generate data at 481 times the productivity of the real LiDAR. Analysis of the approach is presented in the results section. Fig. 7 shows some examples of simulated drones which are inserted in real background. The number of points of each drone is larger than 10 and all drone positions are randomly selected.

The Digital Twin enables the development cycle to virtualize the cost and risk of collecting data in safety critical scenarios such as violations of swarm separation rules and incursions by uncooperative drones.

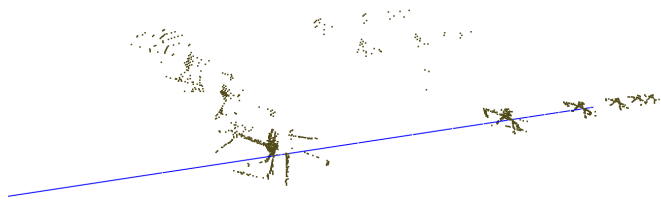


Fig. 6: Synthetic clusters of drones generated by ray tracing

4.2.1 LiDAR simulation with NVIDIA OptiX Ray Tracing

We incorporate the NVIDIA OptiX Ray Tracing engine [48] to accelerate the simulation of the LiDAR, using a GPU

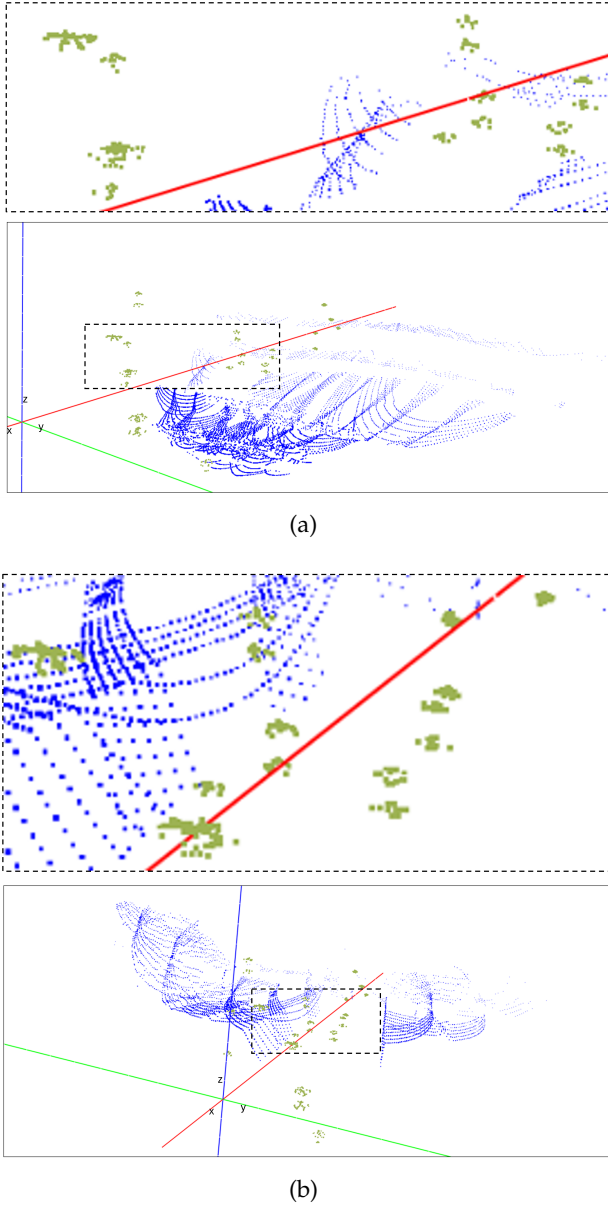


Fig. 7: Visualization of simulated drones (represented as green points) inserted into two different real backgrounds. Each image is divided into two sections: the lower part provides a distant view of the entire scene, while the upper part shows an enlarged view of a selected area.

system equipped with Ray Tracing cores. The OptiX engine utilizes hardware-accelerated data structures, such as the Bounding Volume Hierarchy (BVH), to expedite the ray tracing process. This technology enables the OptiX engine to efficiently traverse complex scenes and accurately compute the intersection of rays with objects. During the simulation process, the mesh model of the target drone will be repeatedly rotated and translated within the LiDAR’s field of view, requiring frequent rebuilding or updating of the acceleration data structure. However, this rebuilding or updating process can be computationally expensive. We propose an alternative approach that eliminates the need for rebuilding or updating the acceleration data structure. This method

allows for a significant reduction in the computational cost of the simulation process.

In the conventional approach, the drone is first rotated, and then the LiDAR ray is projected onto it. This requires rebuilding or updating the acceleration structure within the ray tracing core. However, since rotation and translation are relative in physics, we can instead rotate and translate the LiDAR ray’s origin and direction vector, avoiding the need to rotate and translate the drone mesh model. Specifically, we first align the origin of the LiDAR ray with the origin of the 3D coordinate system, and then align the centerline of the LiDAR’s field of view with the x-axis. Assuming the rotation angle of the drone is θ (note that we do not actually rotate the drone mesh in our implementation), the proposed LiDAR simulation, which bypasses the need to rebuild or update the acceleration structure, involves the following steps:

- **Step 1.** Rotate the direction vectors of the LiDAR ray $-\theta$ degrees around z-axis.
- **Step 2.** Move the origin of the coordinate system to the centre of the drone mesh model.
- **Step 3.** Rotate the origin of the LiDAR ray $-\theta$ degrees around z-axis.
- **Step 4.** Move the origin of the coordinate system to the origin of LiDAR ray.
- **Step 5.** Compute the intersection points between LiDAR rays and drone triangle mesh using OptiX.

Each OptiX thread computes a new ray origin and direction vector independently, rather than rebuilding the acceleration structure in ray tracing core.

For the 3D rotation of a drone triangle mesh, we only consider rotation around the z-axis (up-right). The following rotation matrix is used, where θ is the angle of rotation.

$$\begin{bmatrix} \cos(\theta) & -\sin(\theta) & 0 \\ \sin(\theta) & \cos(\theta) & 0 \\ 0 & 0 & 1 \end{bmatrix}$$

The reflection model used by the DJI L1 Lidar is based on the Lambertian reflection model [49]. This model assumes that the intensity of the reflected laser beam is proportional to the cosine of the angle between the laser beam and the surface normal of the object being scanned,

$$I = IO \times \cos(\alpha) \tag{5}$$

where I is the intensity of the reflected ray, IO is the intensity of the incident ray, and α is the angle between the incident ray and the surface normal.

4.3 Training Parameter

The parameters for the training process are as follows. For a single GPU, we limit the batch size to 4 due to memory constraints. However, when training with 8 GPUs, we increase the batch size to 32. During our experiments, we noticed that after 128 epochs, the accuracy did not improve further. Regarding the learning rate, we deviate from the original PointPillars paper (which used 0.0001) and set it to 0.001. Our empirical observations indicate that this value is more suitable for our use case. Safety is critical in our use case scenario, so we avoid any point cloud sampling. Otherwise, small objects like drones might be excluded

from the scene. In our use case, we have not encountered any situations where sampling out occurs, when we set the maximum number of points each pillar to 100 and the maximum number of pillars to 12,000. However, these two values are changeable, they depend on the use case. To determine the optimal threshold values for positive IoU and negative IoU, we conducted numerous experiments with various combinations. Our observations indicate that the combination of 0.4 for positive IoU and 0.35 for negative IoU yields the highest accuracy.

5 MODEL TEST

5.1 Model Test with Digital Twin

The LiDAR point data is accumulated into time windowed frames and then input to the detection model. The optimal time window depends on several factors. The upper threshold is determined by the acceptable computational latency which increases in proportion to the number of points in each frame, while the lower threshold is determined by the spatial-temporal sensing capability of the LiDAR. To assess the detection model’s performance across different datasets and parameters, we utilize high-fidelity drone and LiDAR simulations within a scenario-based Digital Twin. The selected time window affects the number of points that can be returned from an object within the LiDAR field of view. The heterogeneous LiDAR scanning pattern generates a non-uniform directivity response. This affects the object detection performance, with significant variation in the number of laser-returns backscattered by objects observed at different locations within the LiDAR field of view. The directivity response is a key factor in pre-mission risk assessment as drone observations with sparse point clouds will register as false negatives. Fig. 8 and 9 illustrate the directivity pattern of LiDAR scanning with different time windows and sensing thresholds. The field of view of the LiDAR is discretized into cubic voxels of 1.0m side length. The drone mesh model (see Fig. 4(b)) is placed at centre of each voxel. These voxels are then ray-traced over a time-windowed interval. Voxels that do not achieve the required number of ray intersections are excluded from the visualization. Only the center points of voxels that surpass the threshold are visualized and colored based on the number of intersections, i.e., generated points.

The detection model is tested within the digital twin using different point cloud data obtained from the scenario site with different configurations and varying frame time windows. Our experiments demonstrate that 100ms is an acceptable trade-off between latency and the number of points that are sent to the inference model for analysis.

5.2 Metrics and Error Budget for Model Test

To evaluate the performance of the trained model we use the recall, precision, and F1 scores ($F1$). Recall (R) is the ratio of the number of true positive (TP) examples to the sum of true positives and false negatives (FN) examples. It measures the model’s ability to correctly identify all positive examples out of all the positive examples in the dataset. In the sense and detect use case it is essential to minimize the number of false negatives to ensure the safety of the system

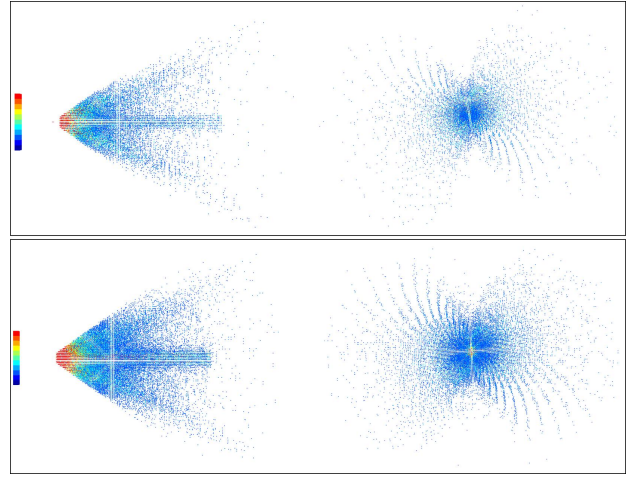


Fig. 8: (top) 100ms scanning time and 4 points per voxel threshold, and (bottom) 200ms scanning time. Each square block in the heat map represents the number of points per voxel threshold. The deep blue box in the bottom indicates that the minimum number of points per voxel is 1. The red box in the top indicates the minimum number of points per voxel is 20.

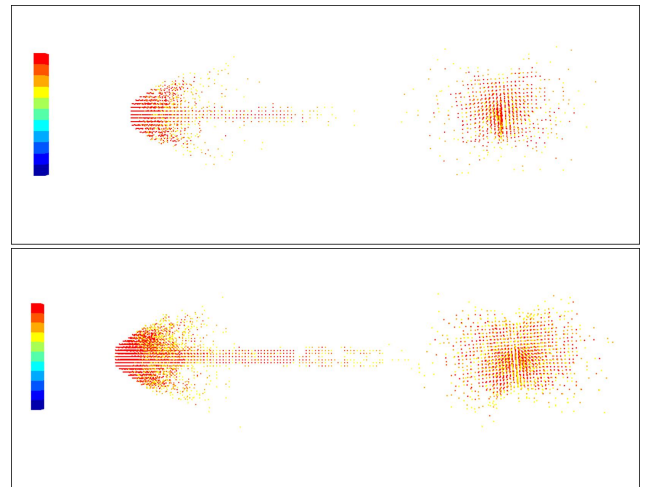


Fig. 9: (top) 100ms scanning time and 14 points per voxel threshold, and (bottom) 200ms scanning time and 14 points per voxel threshold.

and reduce risk of accident due to collision. False negatives mean that an airborne hazard is not detected, leading to a potential mid-air collision.

$$R = \frac{TP}{TP + FN} \tag{6}$$

Precision (P) is the ratio of the number of true positive (TP) examples to the sum of true positives and false positives (FP) examples. It measures the model’s ability to identify only the relevant positive examples out of all the positive predictions. In a sense and detect scenario, false positives occur when the system detects an object or obstacle that is not actually present, leading to unnecessary actions or alerts. Minimizing false positives is important because it

can help reduce the number of unnecessary actions or alerts, which lead to confusion, potentially dangerous actions, and inefficiencies.

$$P = \frac{TP}{TP + FP} \quad (7)$$

The F1 score is the harmonic mean of precision and recall. It is a single metric that balances both precision and recall. A high F1 score means that the model has both high precision and high recall.

$$F1 = 2 \times \frac{P \times R}{P + R} \quad (8)$$

The recall, precision, and F1 score are calculated using IoU (Intersection over Union) scores, which is a measure of the overlap between the predicted bounding box and the ground truth bounding box. The intersection area is the area where the predicted and ground truth regions overlap, while the union area is the total area of both regions. The IoU score is then calculated as:

$$IoU = \frac{Intersection}{Union} \quad (9)$$

We use the following thresholds for IoU measurements:

- True Positive: at least 30% IoU between ground truth and inference bounding boxes.
- False Negative: undetected ground-truth bounding box, i.e. the frame contains a drone.
- False Positive: misplaced detection, i.e. a bounding box is placed in an incorrect location.

The IoU criterion of at least 30% between the inference label and ground truth label is justified by the relative volume of the drone compared within the overall scene. For example, PointPillars models validated on KITTI use a 50% threshold for pedestrians. In addition, incorporating the error budget of the positional estimation extends the volume of the ground truth bounding box label significantly. The error budget of the drone positional estimation can vary from 2-3cm for RTK and PPK solutions up to 10s of meters. For example, an RTK system in convergence mode degrades to 20-30cm accuracy, while if the RTK drops out at any stage, the whole flight reverts to 2-3m DGPS accuracy. As the drone occupies a 1.6m×1.6m×1.0m cube, this challenges ground truth labelling and biases IoU measurements during training, validation, and testing.

While the drones can be required to fly a path that risks denial of GNSS and communications due to multi-path and signal occlusion by large civil engineering infrastructure, a tracking-by-detection algorithm is incorporated into the labelling. The algorithm begins with an initial set of detections performed by the deep learning-based detection algorithm. These detections correspond to objects within the scene and serve as the starting point for subsequent tracking. Bounding boxes are associated with these detected objects, encapsulating each object of interest. The approximate speed of the sentry drone which is equipped with LiDAR for monitoring, is estimated by analyzing the positional change between two consecutive detections. In each

successive frame, the position of tracked objects is estimated by re-centering the bounding box to the centroid of a sparse point cluster, which represents the object's current location. If there are no points inside the re-centered bounding box, the frame is skipped, and the algorithm proceeds to the next frame. The speed information is used for the re-centering process. In practice, the deep learning-based detection algorithm and tracking algorithm are dynamically used. If deep learning-based detection successfully identifies objects in the current frame, we proceed to the next frame. Otherwise, we switch to using a tracking algorithm for that frame. The speed estimation of the sentry drone is updated using the latest two consecutive detections. The integration of tracking with detection aims to minimize both false positives (incorrectly identified objects) and false negatives (missed detections). The results of the strategy are analyzed in the results section.

6 HARDWARE DESIGN AND SYSTEM INTEGRATION

6.1 System Design Requirement

For real-time sense and detect of drone in a safety scenario, the system design must adhere to the following requirements:

- Latency: The frame-to-frame processing time must be minimized to ensure timely responses in dynamic environments.
- Range: The sensor should provide sufficient coverage for reliable detection across the required area.
- Accuracy: The system should achieve high accuracy to ensure that sensor provides reliable detection.
- Independent of external aiding systems: The system should operate effectively without relying on external aids like GNSS. For example, GNSS can introduce errors such as GPS drift [50].
- Localization: The system must support 3D spatial localization to meet the specific requirements of the use case.
- Weight and Power Limitations: The design must accommodate the constraints of drone payload capacity and battery power.

6.2 System Integration

The inference model is embedded on an Nvidia AGX mounted on a DJI M300 drone. The DJI M300 provides a power supply of 96W at 24VDC for the payload and has a 2.7kg payload lift capacity. Our integrated system always weighs less than this limit. The drone's battery provides sufficient power to all hardware components. The AGX and peripherals are enclosed in a weatherproof housing and mounted with 3D printed brackets as shown in Fig. 10. Aside from the PSU requirement, the bolt on system is agnostic of the host drone platform. A collection of power converters provide the required step up/down voltages between the XT30 24VDC supply and the payload electronic components.

The perception sensor is a Livox Avia LiDAR and it is connected to the AGX computer via a network hub. The network hub provides a bi-directional communications link to the ground via a Wi-Fi antenna mounted on the drone

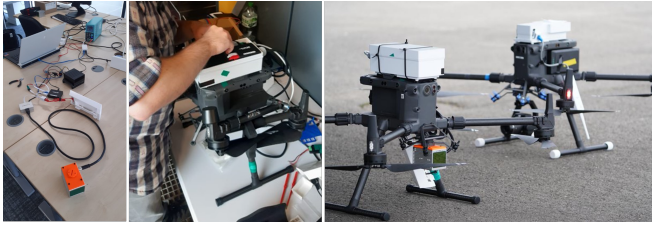


Fig. 10: Our real-time embedded system for object detection

chassis. This enables the software running on the AGX to send alert messages to the pilot on the ground over a TCP-IP socket. An XRDP remote desktop protocol agent enables the operator to configure the onboard components during pre-flight checks. Before take-off the XRDP is disconnected to minimize bandwidth and GPU load and the TCP-IP network socket is launched to provide alerts to ground. The system schematic is shown in Fig. 11.

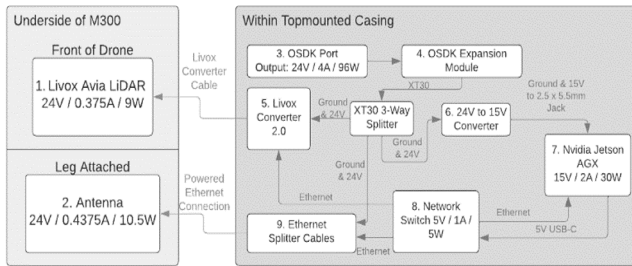


Fig. 11: Illustration of the real-time system schematic

While a higher number of point clouds can boost detection accuracy, low latency is essential for real-time hazard response. According to [51], the Avia LiDAR is capable of covering most of the field of view (FOV) in 0.1 seconds (100 milliseconds). On the other hand, our experiments demonstrate that a latency of 100ms achieves an effective balance between two competing factors: ensuring sufficient accuracy and delivering a timely response for safety. Through experimentation, we determine that the system’s maximum detection range is roughly 68m. To comprehensively assess the accuracy of our drone detection system in safety-critical scenarios, our evaluation considers three key metrics: precision, recall, and F1-score.

In safety-critical applications, the system must be independent of external aiding systems like GNSS positioning. Since GNSS multipath errors (bouncing off buildings, tree and ground etc.) may cause positioning errors such as GPS drift. By deploying the detection model directly on the drone, we eliminate the need for external aiding systems.

The designed system provides accurate 3D localization to determine the separation distance between drones within a swarm. The system successfully alerts the remote pilot if two drones come so close to each other as to violate the minimum separation rule of the operating theatre. While strategic conflict management is achieved through mission planning and pre-flight risk management, this level of tactical deconfliction is required as drones often need to deviate from pre-planned flight paths in response to an incursion by uninvolved persons, or an unscheduled return to home event due to battery depletion etc.

7 RESULTS

7.1 Performance of Sparse Convolution with Scatter Operation

We use different experiments to evaluate the proposed sparse convolution with scatter operation. An NVIDIA Jetson Xavier (32GB SSD) and JetPack 5.0.2 with CUDA 11.4 is used for the performance evaluation. The original PointPillars implementation [52] utilizes cuDNN’s dense convolution for the backbone layer. We compare the performance of our sparse convolution approach with that of the cuDNN dense convolution. As shown in Fig 12, our sparse convolution demonstrates significant performance improvements compared to the dense convolution in cuDNN. Notably, as the number of input channels increases, the performance gains become more significant. This is possibly because, when the number of input channels is small, the scattering step dominates the processing time, and its reliance on atomicAdd() operations results in slower performance. However, as the number of input channels grows, the matrix multiplication step becomes the dominant factor in processing time, benefiting from the efficient implementation provided by cuBLAS.

We implemented the backbone layer of the detection model using sparse convolution with a scatter operation and evaluated its performance on real LiDAR data consisting of 1,000 frames. The backbone layer comprises three convolution blocks and three deconvolution (transposed convolution) operations. Each convolution block contains 4, 6, and 6 convolutions, respectively. Our sparse convolution is used to implement both the convolutions and deconvolutions within the backbone. Experiments show that our sparse convolution reduces inference time by 28.5%. However, this reduction falls short of our expectations. This is because, while the initial convolutions operate on sparse data, the majority of subsequent convolutions process dense data due to the expansion property inherent in the convolution operation. To mitigate the expansion caused by the convolution operation, the submanifold sparse convolution is employed in each convolution block, except for the first convolution of each block. The submanifold sparse convolution is implemented using the scatter operation. Experiments show that inference can be accelerated by a factor of 2.3 when the submanifold sparse convolution is employed.

7.2 Model Performance Across Different Use Cases

To evaluate the sense and detect system, the embedded model was tested during supervised flights at Newcastle Aerodrome, Ireland (Fig. 13) and Hamburg Port, Germany (Fig. 14). The two test sites comprise a mix of built and natural environment and provide distinct background scenery from one another. The Newcastle site is a coastal railway bridge over a tidal inlet and is surrounded by rocks, gravel, and sand dunes. The Hamburg site is the Harburg Lock, which is a navigable waterway system that consists of a concrete chamber with gates at either end, surrounded by buildings and trees. Maintenance inspection surveys were performed at both sites involving multiple drones deployed with camera and LiDAR sensors to collect point and pixel datasets for structural analysis. The flight profiles at both

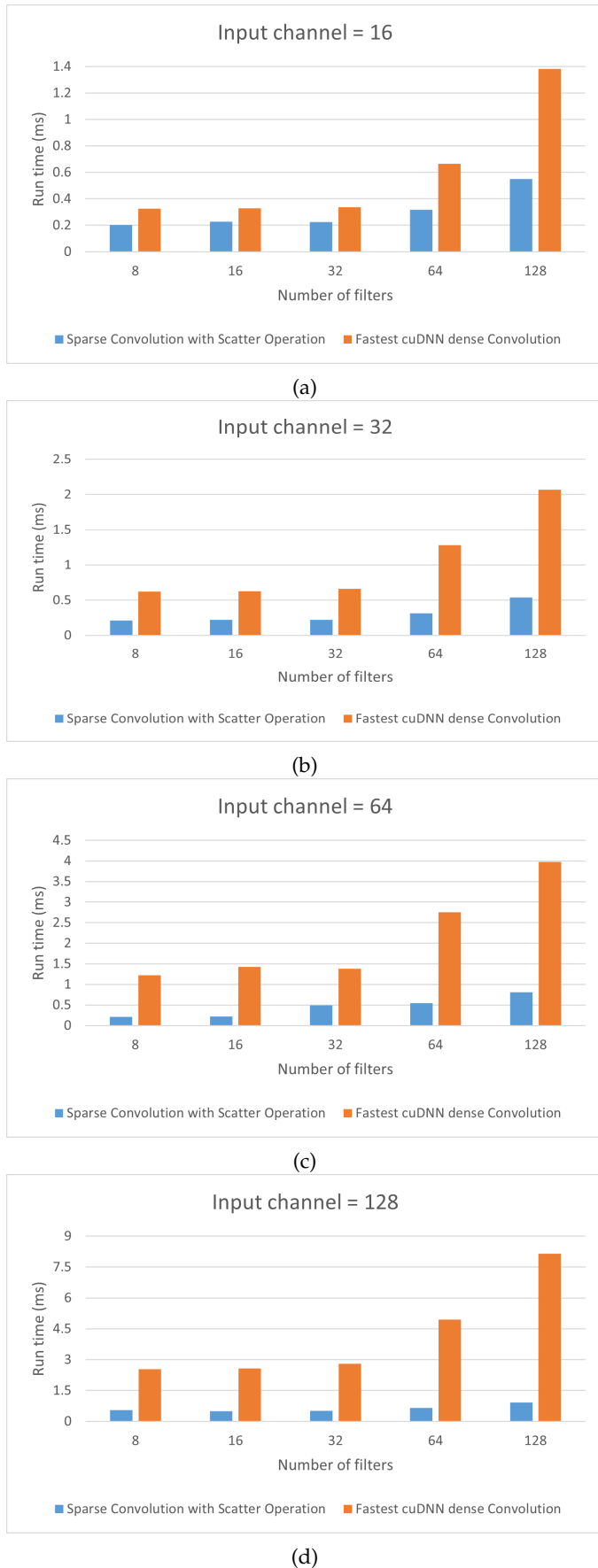


Fig. 12: Performance of convolutions with varying parameters, evaluated over 1,000 images, with an average of 5,124 active sites per image; Size of image = 504×504 , filter size = 3×3 .

sites were also significantly different, in particular the perspective and relative vantage points from which drones were observed in the LiDAR training data. This is significant as the detection model decorates input points to encode the shape, appearance, and relative position of observed objects, while the grid and pillar layout encodes the spatial relationship between the object and its surrounding environment.



Fig. 13: Test site 1: The railway bridge 1.5km north of Newcastle Aerodrome (EINC), County Wicklow, Ireland.



Fig. 14: Test site 2: The Harburger-Lock, Hamburg, Germany.

The data specification of maintenance inspection surveys facilitates swarm flights as multiple drones can simultaneously fly spatially segmented waypoint- and route-based data collection missions as the different point- and pixel-datasets have different resolution requirements. For example, collection of sub mm Ground Sample Density camera imagery in photogrammetry and crack detection use cases can require the drone to fly within 2-6m of the target structure etc., while LiDAR surveys aiming for cm point density can fly at offset distances of 20-30m. This facilitates separation and deconfliction of planned swarm trajectories during strategic flight risk management.

7.2.1 Experiment 1: Newcastle use case

The Newcastle scenario involved two drones deployed to survey the railway bridge, one drone carrying a LiDAR sensor and the other with a high-resolution camera for photogrammetry, see Fig. 15. The LiDAR flight was approximately 10 minutes duration, including IMU calibrations

at the start and end of the mission. The LiDAR drone frequently observed the camera drone, with observations in the point cloud data annotated using positional information extracted from the flight logs. The objective was to evaluate the performance of the model and the data augmentation strategy.



Fig. 15: Newcastle scenario: Two drones deployed to survey the railway bridge. The red arrow indicates the target drone in the image captured by the camera of the sentry drone (monitoring drone). The small picture inside the image is captured by the high resolution camera of photogrammetry drone.

The collected LAS dataset (*data_orig*) was segmented into 100ms frames, and the target drone observations were labelled with bounding boxes placed at locations derived from the target drone flight log. The dataset was then reduced into the set of frames (N=1603) that contained bounding boxes enclosing at least 10 points. The first 400 instances (*real_first_400_frame*) of the resulting frames were filtered to extract observations of the target drone and the background separately. We call them (*extracted_drone*) and (*extracted_background*) respectively.

The detection model (*model_real*) was trained on the 1603 real frames first. Then the detection model was trained on different datasets which are generated by different augmentation strategies.

For our augmentation strategy, a LiDAR simulation space was generated by stratifying the volume enclosed by the LiDAR FOV at 1m intervals vertically and horizontally. The 3D mesh model of the drone was then placed at the centre of each discrete $1m^3$ cell (at random orientations) and ray tracing by the LiDAR simulator for the equivalent time of 100ms. The simulated point clusters (N=2495) were retained at locations that generated at least ten ray tracing hits. Each of the 2495 instances was then randomly matched to one of the 400 backgrounds (*extracted_background*). The resulting dataset (*data_sim*) and the real 400 frames (*real_first_400_frame*) were used together to train the detection model (*model_sim*). The set of insertions locations was retained and reused in generating a comparative dataset from Euclidean augmentations in the second strategy.

To generate the Euclidean augmentation dataset (*data_euc*), each instance of (*extracted_drone*) were up-sampled into 2895 exemplars by creating 2495 additional

rotated copies. Each point cluster was then translated to the corresponding background and insertion locations retained during construction of the *data_sim* dataset. The resulting dataset (*data_euc*) was used to train the detection model (*model_euc*).

Both datasets are the same size, contain the same number of augmentations, and corresponding frames have the same background with a drone inserted in the same location. To test the performance of the respective models, we collected new LiDAR data from the same mission site, which consists of consecutive 2694 frames. In these 2694 frames, drones (ground truth) observed in 1555 frames. The model was evaluated by measuring the number of true positives, false negatives, and false positives to calculate the recall (TP/TP+FN) and precision (TP/TP+FP).

As shown in Table 1, the model trained on a point cloud consisting of both simulated data (*data_sim*) and real data from the first 400 frames (*real_first_400_frame*), without utilizing intensity values, achieves the best performance in all of the evaluation metrics, Precision, Recall, and F1 score. However, the model's performance decreases when intensity values are used for training, indicating that there is a discrepancy between the the simulated intensity values and the ground truth intensity values. The model trained on a point cloud generated by combining Euclidean augmentation of real data, specifically (*data_euc*) and (*real_first_400_frame*), without utilizing intensity values, achieves a competitive performance. The model's performance decreases when using intensity values for training, potentially due to the aforementioned possible discrepancy. The model trained on real data without any modifications achieves a comparable performance. However, it produces more false negatives, suggesting a lower capability for detecting drones. These results demonstrate that our simulation augmentation strategy can generate more accurate data than Euclidean augmentation of real data.

Visualization of both predicted bounding box and ground truth bounding box is shown in Fig. 16, where the inference model applied is (*model_sim*). Through our testing, we discovered that, predicting the heading of the detected drone is the most challenging task. This could be attributed to the fact that heading prediction typically requires a sufficient number of points representing the geometric structure of the body of the drone. However, in most cases, the LiDAR cannot generate an adequate number of points, because the drone is such a small object. In certain instances, as depicted in Fig. 16(c), there is a noticeable difference between the center of the predicted bounding box and that of the ground truth bounding box. This observation suggests that our model is imperfect.

7.2.2 Experiment 2: Hamburg use case

Testing at Harburg Lock, Hamburg, Germany involved an inspection survey with two drones simultaneously flying LiDAR (circled green) and camera (circled red) data capture missions, see Fig. 17. The camera drone mission was to capture imagery of the Lock wall with c. 1mm Ground Sample Distance, flying within Lock chamber to a distance of 1-2m of the Lock wall (equipped with a 45MP camera) while oriented towards the wall. The LiDAR drone flew c.

TABLE 1: Evaluation of the detection model on Newcastle dataset

Trained model	Training dataset	Intensity value	Precision	Recall	F1 score
model_sim	<i>(data_sim)</i> i.e. 2495 frames each frame is created by inserting simulated drone in real background + <i>(real_first_400_frame)</i> i.e. the first 400 frames of 1603 real frames	applied	0.523	0.75	0.616
		not applied	0.96	0.80	0.872
model_euc	<i>(data_euc)</i> i.e. 2495 frames each frame is created by inserting real drone in real background, where each real drone is extracted from the first 400 frames of 1603 real frames, and Euclidean transform is applied to each drone + <i>(real_first_400_frame)</i> i.e. the first 400 frames of 1603 real frames	applied	0.24	0.774	0.367
		not applied	0.766	0.513	0.614
model_real	1603 real frames collected from real drone fly	applied	0.826	0.62	0.706

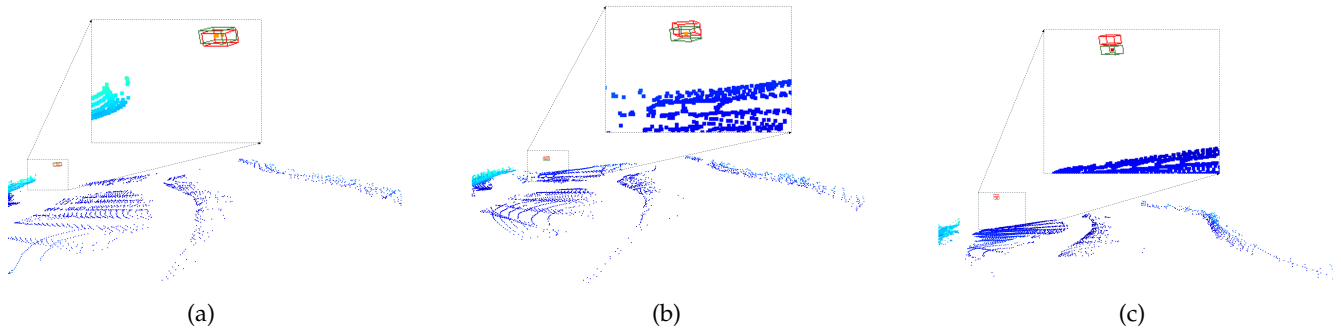


Fig. 16: Visualization of predicted bounding box (red) and ground truth bounding box (green), the inference model used is (*model_sim*) described in Table 1, a portion of the frame containing the drone is enlarged for clarity. (a) The predicted bounding box has a good overlap with the ground truth bounding box (b) The predicted heading is different with the ground truth (c) The difference between the centre of predicted bounding box and the centre of ground truth bbox is significant.



Fig. 17: Harburg Lock scenario: Two drones (circled red and green) deployed for an inspection survey, the third drone is (circled yellow) monitoring their separation distance.

10m above the sentry drone (circled yellow) which is for monitoring, in a high altitude 2-dimensional lawnmower style pattern that divided the survey area into a series of parallel strips and the drone flew each strip in a systematic back-and-forth manner.

While the flight plans for both drones were strategically separated using trajectory-based planning, the camera drone was required to fly a runline that risked denial of GNSS and communications due to multi-path and signal occlusion by the walls of the lock chamber. The operational risk management incorporated additional controls to monitor and track the drones during scheduled close encounters and to mitigate against potential air-to-air collision in the event of unplanned deviations. Potential trigger events in-

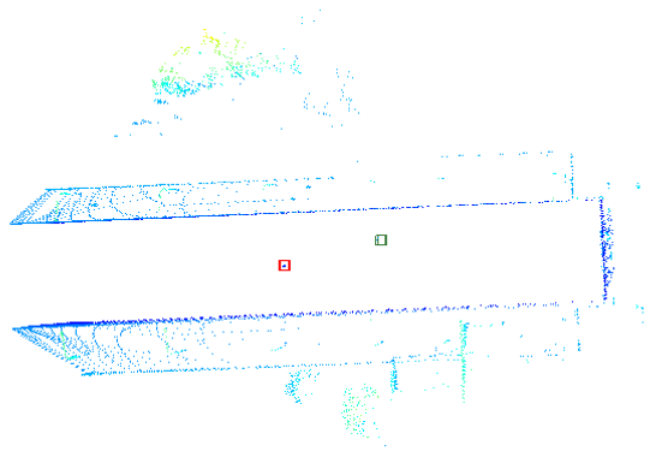


Fig. 18: Detection of two drones using the sense and detect system. The red bounding box is predicted by the deep-learning based detection model and the green bounding box is by the tracking algorithm

cluded incursions by people or vehicles and return-to-home events due to battery depletion.

A drone equipped with a Livox Avia LiDAR and the sense and detect system was deployed to monitor the two survey drones. The system was configured to raise an alert once a minimum separation threshold was breached, in this instance when the survey drones came within 15m of each other. The sentry drone (monitoring drone) was positioned to station keep at one end of the Lock and at a flight elevation midway between the two survey drones. Fig. 18

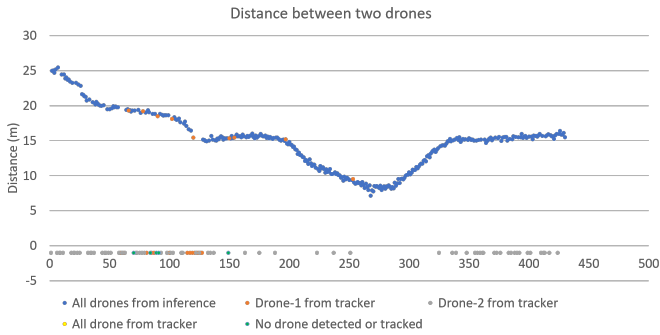


Fig. 19: Distance between the two drones fly-by, where the distance is computed using the detection results of detection and tracking algorithm

shows a 100ms frame in which two drones are detected by the system.

The detection model was trained on data that was previously captured in the Lock and augmented with synthetic observations using the digital twinning method described earlier. The 100ms point cloud scenes presented to the detection model embedded on the sentry drone (monitoring drone) typically contained observations of the LiDAR drone positioned relatively high and well clear of other objects, as well as the camera drone positioned relatively low and near the concrete wall. The surrounding environment was complex, cluttered, and dynamic encompassing people, buildings, trees and vegetation, as well as a wide range of building and man-made objects (e.g. lamp posts). Both drones tended to appear at the periphery of the usable field of view of the LiDAR of the sentry drone.

The sense and detect system combined the deep-learning based detection model with the tracking-by-detection algorithm described earlier. Fig. 19 displays a graph of the distance between the two drones during an example close encounter and fly-by.

The quantitative data is presented in Table 2. There are 430 frames in total, representing 43 seconds of flight perception data and translating to an average relative speed of c. 1m/s between the two drones.

As shown, the combination of the deep-learning based detection model and the detection-by-tracking algorithm enables the sense and detect system to robustly track the positions of two drones. The solution accuracy is the range resolution of the LiDAR, in this case 5cm, which is comparable with RTK GPS solutions. As it is a relative based positioning and deconfliction system it is robust to drop out of satellite coverage, while the ability to automatically track dynamic objects compares favorably to a ground based total station.

TABLE 2: Quantitative data associated with graph in Fig. 19.

Two drones tracked by inference model detection	333
Two drones tracked by combination of inference model (1) and tracker algorithm (1)	9
Only one drone tracked by either method	83
No drones detected or tracked	5

8 CONCLUSION

This paper tackles the challenge of monitoring a drone swarm during collaborative tasks. It presents the first drone-embedded system that employs point-based deep learning for detecting and localizing other drones. We adapt an existing detection model, originally designed for ground applications, to an air-to-air drone scenario by expanding the scan space vertically. To reduce the latency of the detection model, we propose a new sparse convolution algorithm that improves efficiency by bypassing the mapping between input and output, which is required by existing methods. This algorithm accelerates the model’s backbone layer, which is the most time-consuming component of the detection process. A scenario Digital Twin implemented to simulate close encounters and safety-critical scenarios to gather training data. By augmenting the actual background data with high-quality synthetic drone data, we improve the accuracy and efficiency of our training and inferencing processes. Moreover, we incorporate a tracking-by-detection algorithm into the system, which allows for accurate monitoring of the separation distance of multiple drones, even in challenging environments.

Our approach has been successfully validated through real-world tests, with the trained model achieving an impressive 80% recall and 96% precision when tested on real datasets. We trained the detection model on several datasets, each generated using different augmentation strategies, and found that our simulation augmentation strategy produced more precise data than the conventional augmentation method used with real data. Overall, our proposed approach offers a novel and effective solution for drone swarm detection and localization, with promising results from our tests.

ACKNOWLEDGMENTS

This work was funded by the European Commission under project RAPID (risk-aware port inspection drones, 2020-2023) which is funded through the Horizon 2020 research and innovation programme and Grant Agreement number 861211.

REFERENCES

- [1] G. Fasano, D. Accado, A. Moccia, and D. Moroney, “Sense and avoid for unmanned aircraft systems,” *IEEE Aerospace and Electronic Systems Magazine*, vol. 31, no. 11, pp. 82–110, 2016.
- [2] A. Hommes, A. Shoykhetbrod, D. Noetel, S. Stanko, M. Laurenzis, S. Hengy, and F. Christnacher, “Detection of acoustic, electro-optical and radar signatures of small unmanned aerial vehicles,” in *Target and Background Signatures II*, vol. 9997. SPIE, 2016, p. 999701.
- [3] D. Tejera-Berengue, F. Zhu-Zhou, M. Utrilla-Manso, R. Gil-Pita, and M. Rosa-Zurera, “Acoustic-Based Detection of UAVs Using Machine Learning: Analysis of Distance and Environmental Effects,” in *2023 IEEE Sensors Applications Symposium (SAS)*. IEEE, 2023, pp. 1–6.
- [4] P. Nguyen, V. Kakaraparthi, N. Bui, N. Umamahesh, N. Pham, H. Truong, Y. Guddeti, D. Bharadia, R. Han,

- E. Frew, D. Massey, and T. Vu, "DroneScale: drone load estimation via remote passive RF sensing," in *Proceedings of the 18th Conference on Embedded Networked Sensor Systems*. New York, NY, USA: Association for Computing Machinery, 2020, p. 326–339.
- [5] M. Caris, S. Stanko, W. Johannes, S. Sieger, and N. Pohl, "Detection and tracking of micro aerial vehicles with millimeter wave radar," in *2016 European Radar Conference (EuRAD)*, 2016, pp. 406–408.
- [6] Á. D. de Quevedo, F. I. Urzaiz, J. G. Menoyo, and A. A. López, "Drone detection and radar-cross-section measurements by rad-dar," *IET Radar, Sonar & Navigation*, vol. 13, no. 9, pp. 1437–1447, 2019.
- [7] H. Arroyo, P. Keir, D. Angus, S. Matalonga, S. Georgiev, M. Goli, G. Dooly, and J. Riordan, "Segmentation of drone collision hazards in airborne radar point clouds using pointnet," *IEEE Transactions on Intelligent Transportation Systems*, vol. 25, no. 11, pp. 17762–17777, 2024.
- [8] C. Aker and S. Kalkan, "Using deep networks for drone detection," in *2017 14th IEEE International Conference on Advanced Video and Signal Based Surveillance (AVSS)*. IEEE, 2017, pp. 1–6.
- [9] A. Rozantsev, V. Lepetit, and P. Fua, "Detecting flying objects using a single moving camera," *IEEE Transactions on Pattern Analysis and Machine Intelligence*, vol. 39, no. 5, pp. 879–892, 2017.
- [10] E. Unlu, E. Zenou, N. Riviere, and P.-E. Dupouy, "Deep learning-based strategies for the detection and tracking of drones using several cameras," *IPSA Transactions on Computer Vision and Applications*, vol. 11, no. 1, pp. 1–13, 2019.
- [11] J. Li, D. H. Ye, M. Kolsch, J. P. Wachs, and C. A. Bouman, "Fast and robust uav to uav detection and tracking from video," *IEEE Transactions on Emerging Topics in Computing*, vol. 10, no. 3, pp. 1519–1531, 2022.
- [12] M. Hammer, B. Borgmann, M. Hebel, and M. Arens, "A multi-sensorial approach for the protection of operational vehicles by detection and classification of small flying objects," in *Security + Defence*, 2020.
- [13] F. Causa, R. Opromolla, and G. Fasano, "Closed loop integration of air-to-air visual measurements for cooperative UAV navigation in GNSS challenging environments," *Aerospace Science and Technology*, vol. 130, p. 107947, 2022.
- [14] Y. Guo, H. Wang, Q. Hu, H. Liu, L. Liu, and M. Benamoun, "Deep Learning for 3D Point Clouds: A Survey," *IEEE Transactions on Pattern Analysis and Machine Intelligence*, vol. 43, no. 12, pp. 4338–4364, 2021.
- [15] R. Charles, H. Su, M. Kaichun, and L. J. Guibas, "PointNet: Deep Learning on Point Sets for 3D Classification and Segmentation," in *2017 IEEE Conference on Computer Vision and Pattern Recognition (CVPR)*, Los Alamitos, CA, USA, 2017, pp. 77–85.
- [16] C. R. Qi, L. Yi, H. Su, and L. J. Guibas, "PointNet++: Deep Hierarchical Feature Learning on Point Sets in a Metric Space," in *Proceedings of the 31st International Conference on Neural Information Processing Systems*, 2017, pp. 5105–5114.
- [17] Y. Zhou and O. Tuzel, "VoxelNet: End-to-end learning for point cloud based 3d object detection," in *Proceedings of the IEEE conference on computer vision and pattern recognition*, 2018, pp. 4490–4499.
- [18] Y. Yan, Y. Mao, and B. Li, "SECOND: Sparsely Embedded Convolutional Detection," *Sensors*, vol. 18, no. 10, 2018.
- [19] J. Deng, S. Shi, P. Li, W. Zhou, Y. Zhang, and H. Li, "Voxel r-cnn: Towards high performance voxel-based 3d object detection," in *Proceedings of the AAAI Conference on Artificial Intelligence*, vol. 35, no. 2, 2021, pp. 1201–1209.
- [20] A. H. Lang, S. Vora, H. Caesar, L. Zhou, J. Yang, and O. Beijbom, "Pointpillars: Fast encoders for object detection from point clouds," in *Proceedings of the IEEE/CVF Conference on Computer Vision and Pattern Recognition (CVPR)*, 2019, pp. 12697–12705.
- [21] W. Liu, D. Anguelov, D. Erhan, C. Szegedy, S. Reed, C.-Y. Fu, and A. C. Berg, "SSD: Single shot multibox detector," in *Computer Vision—ECCV 2016: 14th European Conference, Amsterdam, The Netherlands, October 11–14, 2016, Proceedings, Part I 14*. Springer, 2016, pp. 21–37.
- [22] S. Shi, X. Wang, and H. Li, "PV-RCNN: Point-Voxel Feature Set Abstraction for 3D Object Detection," in *Proceedings of the IEEE/CVF Conference on Computer Vision and Pattern Recognition*, 2020, pp. 10529–10538.
- [23] K. Lis and T. Kryjak, "Pointpillars backbone type selection for fast and accurate lidar object detection," 2022.
- [24] B. Graham, "Spatially-sparse convolutional neural networks," *arXiv preprint arXiv:1409.6070*, 2014.
- [25] B. Liu, M. Wang, H. Foroosh, M. Tappen, and M. Pensky, "Sparse convolutional neural networks," in *2015 IEEE Conference on Computer Vision and Pattern Recognition (CVPR)*, 2015, pp. 806–814.
- [26] B. Graham, M. Engelcke, and L. van der Maaten, "3d semantic segmentation with submanifold sparse convolutional networks," 2017.
- [27] S. Chetlur, C. Woolley, P. Vandermersch, J. Cohen, J. Tran, B. Catanzaro, and E. Shelhamer, "cudnn: Efficient primitives for deep learning," *arXiv preprint arXiv:1410.0759*, 2014.
- [28] C. Choy, J. Gwak, and S. Savarese, "4d spatio-temporal convnets: Minkowski convolutional neural networks," 2019.
- [29] H. Tang, S. Yang, Z. Liu, K. Hong, Z. Yu, X. Li, G. Dai, Y. Wang, and S. Han, "Torchsparse++: Efficient training and inference framework for sparse convolution on gpu," in *IEEE/ACM International Symposium on Microarchitecture (MICRO)*, 2023.
- [30] A. Geiger, P. Lenz, C. Stiller, and R. Urtasun, "Vision meets robotics: The kitti dataset," *The International Journal of Robotics Research*, vol. 32, no. 11, pp. 1231–1237, 2013.
- [31] P. Sun, H. Kretzschmar, X. Dotiwalla, A. Chouard, V. Patnaik, P. Tsui, J. Guo, Y. Zhou, Y. Chai, B. Caine *et al.*, "Scalability in perception for autonomous driving: Waymo open dataset," in *Proceedings of the IEEE/CVF conference on computer vision and pattern recognition*, 2020, pp. 2446–2454.
- [32] H. Caesar, V. Bankiti, A. H. Lang, S. Vora, V. E. Liong, Q. Xu, A. Krishnan, Y. Pan, G. Baldan, and O. Beijbom, "nusenes: A multimodal dataset for autonomous driving," in *Proceedings of the IEEE/CVF conference on computer vision and pattern recognition*, 2020, pp. 11621–

- 11 631.
- [33] H. Abu Alhaija, S. K. Mustikovela, L. Mescheder, A. Geiger, and C. Rother, "Augmented reality meets computer vision: Efficient data generation for urban driving scenes," *International Journal of Computer Vision*, vol. 126, pp. 961–972, 2018.
- [34] Ros, German and Sellart, Laura and Materzynska, Joanna and Vazquez, David and Lopez, Antonio M, "The synthia dataset: A large collection of synthetic images for semantic segmentation of urban scenes," in *Proceedings of the IEEE conference on computer vision and pattern recognition*, 2016, pp. 3234–3243.
- [35] S. R. Richter, V. Vineet, S. Roth, and V. Koltun, "Playing for data: Ground truth from computer games," in *Computer Vision—ECCV 2016: 14th European Conference, Amsterdam, The Netherlands, October 11–14, 2016, Proceedings, Part II 14*. Springer, 2016, pp. 102–118.
- [36] A. Shafaei, J. J. Little, and M. Schmidt, "Play and learn: Using video games to train computer vision models," *arXiv preprint arXiv:1608.01745*, 2016.
- [37] T. Hanke, A. Schaermann, M. Geiger, K. Weiler, N. Hirsenkorn, A. Rauch, S.-A. Schneider, and E. Biebl, "Generation and validation of virtual point cloud data for automated driving systems," in *2017 IEEE 20th International Conference on Intelligent Transportation Systems (ITSC)*. IEEE, 2017, pp. 1–6.
- [38] J. Fang, D. Zhou, F. Yan, T. Zhao, F. Zhang, Y. Ma, L. Wang, and R. Yang, "Augmented lidar simulator for autonomous driving," *IEEE Robotics and Automation Letters*, vol. 5, no. 2, pp. 1931–1938, 2020.
- [39] J. Fang, F. Yan, T. Zhao, F. Zhang, D. Zhou, R. Yang, Y. Ma, and L. Wang, "Simulating LIDAR point cloud for autonomous driving using real-world scenes and traffic flows," *arXiv preprint arXiv:1811.07112*, vol. 1, 2018.
- [40] S. Manivasagam, S. Wang, K. Wong, W. Zeng, M. Sazanovich, S. Tan, B. Yang, W.-C. Ma, and R. Urtasun, "Lidarsim: Realistic lidar simulation by leveraging the real world," in *Proceedings of the IEEE/CVF Conference on Computer Vision and Pattern Recognition*, 2020, pp. 11 167–11 176.
- [41] J. Riordan, M. Manduhu, J. Black, A. Dow, G. Dooly, and S. Matalonga, "Lidar simulation for performance evaluation of uas detect and avoid," in *2021 International Conference on Unmanned Aircraft Systems (ICUAS)*, 2021, pp. 1355–1363.
- [42] NVIDIA Cooperation, "Thrust Prefix Sums documentation," 2023. [Online]. Available: https://thrust.github.io/doc/group_prefixsums.html
- [43] —, "cuBLAS documentation," 2023. [Online]. Available: <https://docs.nvidia.com/cuda/cublas/>
- [44] —, "CUDA C/C++ Programming Guide," 2019. [Online]. Available: <https://docs.nvidia.com/cuda/cuda-c-programming-guide/>
- [45] European Union Aviation Safety Agency. Specific Operations Risk Assessment (SORA). [Online]. Available: <https://www.easa.europa.eu/en/domains/drones-air-mobility/operating-drone/specific-category-civil-drones/specific-operations-risk-assessment-sora>
- [46] DJI. DJI L1 LiDAR. [Online]. Available: <https://www.dji.com/uk/zenmuse-l1>
- [47] Livox Technology Company. Livox Avia. [Online]. Available: <https://www.livoxtech.com/avia>
- [48] NVIDIA. NVIDIA OptiX™ Ray Tracing Engine. [Online]. Available: <https://developer.nvidia.com/rtx/ray-tracing/optix>
- [49] F. Losasso, "Surface reflection models," *NVIDIA Corporation*, vol. 2, 2004.
- [50] K. Kim, W. Kim, D. Choi, and H. Myung, "Calibration of the drift error in GPS using optical flow and fixed reference station," in *2015 15th International Conference on Control, Automation and Systems (ICCAS)*, 2015, pp. 1370–1373.
- [51] LIVOX. Livox Introduces High Performance, Low Cost, Mass Market Lidar Sensors For L3/L4 Autonomous Driving Applications. [Online]. Available: <https://www.livoxtech.com/news/4>
- [52] OpenPCDet. [Online]. Available: <https://github.com/open-mmlab/OpenPCDet>



Manduhu Manduhu received the M.Sc. and Ph.D. degrees in information engineering from Hiroshima University, Japan, in 2010 and 2013, respectively. He is currently a PostDoc researcher at the Drone Systems Lab of the University of the West of Scotland. His research interests include parallel algorithm, physics simulation and 3D object detection.



Alexander Dow is a PhD student at the Drone Systems Lab of the University of the West of Scotland. His research focuses on real-time LiDAR-based object detection for UAVs. He holds a BSc in Sound Engineering and Production from Birmingham City University (2016), and an MSc in Digital Signal and Image Processing from the University of Sussex (2020).



Petar Trsljic is a PostDoc researcher at the CRIS of the University of Limerick (UL). He received both his BSc and MSc degrees in Mechanical Engineering from the University of Zagreb. Petar finished his PhD at UL in March 2020. During his PhD, he was working on the development of advanced monitoring, control systems and onboard robotics for the automation of MRE inspection, repair and maintenance.



Gerard Dooly received the B.Eng. degree from the Electronic and Computer Engineering Department, University of Limerick, in 2003, and the Ph.D. degree from the Optical Fibre Sensors Research Centre, University of Limerick, in 2008, on the topic “An Optical Fibre Sensor for the Measurement of Hazardous Emissions from Land Transport Vehicles.” For over ten years, he has worked extensively in field robotics at UL. His research interests include real-time 3-D re-

construction, machine vision, machine learning, optical fibre sensors, subsea structural health monitoring, teleoperation, and automated docking and intervention. He is involved in robotics for harsh environments in offshore setting and is developing systems to address beyond visual line of sight operations for UAS. He is focused on the design and development of robotics and has engaged in numerous field operations and survey missions both in Ireland and on the continent. Some of his recent offshore operations involved environmental sensing, anti-mine countermeasure ops, remote UAS for incident response, archaeological survey, and hybrid long range UAS technologies.



Benjamin Blanck is a project manager at the Hamburg Port Authority and a master’s student at the University of Hamburg for the ITMC (IT Management and Consulting) course. His focus in studies and work is digitalization projects in the port of Hamburg, as well as Artificial Intelligence and Data Engineering practices. He holds a Bachelor of Science in business informatics from the University of Hamburg (2016) where he focused his studies on resilience in IT companies.



James Riordan received the B.Eng. degree in Electronic Engineering specialising in aircraft simulation systems, and the Ph.D. degree in real-time processing of acoustic signals, both from the University of Limerick, Ireland. Currently, he is a Full Professor at the University of the West of Scotland, U.K., where he is the Director of the Drone Systems Laboratory. He is Principal Investigator of multiple research projects funded by the European Commission and UK Research and Innovation. His research

interests include artificial intelligence, computer vision, and sensing methods to extend the safe and sustainable application of autonomous vehicles in land, air, and sea. specialises in robotics and sensing and is an expert in autonomous vehicles applied to land, air, and sea domains. He is a Professor at University of the West of Scotland where he leads an €8 million portfolio of research projects as Principal Investigator and founding Director of the Drone Systems Lab. He is PI of the European Commission H2020 project RAPID and is an independent external expert to the European Union Aviation Safety Agency. Dr. Riordan has a PhD in underwater sonar modelling and simulation from University of Limerick, Ireland. He has established and successfully commercialised several strands of patented research and has been recipient of 3 national awards for research and innovation.